2015 IEEE/RSJ International Conference on Intelligent Robots and Systems (IROS)
Congress Center Hamburg
Sept 28 - Oct 2, 2015. Hamburg, Germany

Design and Analysis of A Magnetic Actuated Capsule Camera Robot for Single Incision Laparoscopic Surgery

Xiaolong Liu[1] and Gregory J. Mancini[2] and Jindong Tan[1]

Abstract— **This paper presents the design of a novel insertable robotic capsule camera system for single incision laparoscopic surgery. This design features a unified mechanism for anchoring, navigating, and rotating an insertable camera by externally generated rotational magnetic field. The design is inspired by the spherical motor concept where the external stator generates anchoring and rotational magnetic field to control the motion of the insertable robotic capsule camera. The insertable camera body, which has no active locomotion mechanism onboard, is capsulated in a one-piece housing with two ring-shaped tail-end magnets and one cylindrical central magnet embedded on-board as a rotor. The stator positioned outside an abdominal cavity consists of both permanent magnets and electromagnetic coils for generating reliable rotational magnetic field. The initial prototype results in a compact insertable camera robot with a** 12.7 mm **diameter and a** 68 mm **length. The design concepts are analyzed theoretically and verified experimentally. The experiments validate that the proposed capsule robot design provides reliable camera fixation and locomotion capabilities under various testing conditions.**

I. Introduction

SINGLE Incision Laparoscopic Surgery (SILS) is a popular minimally invasive surgery technique. Its benefits include less bleeding, less post-operative pain, faster incision recovery, and better cosmetic results compared with multiport surgeries [1]–[3]. However, a single incision limits the manipulation and triangulation of surgical instruments, especially for a conventional long-stick laparoscopic camera. To solve this problem, manually maneuvered insertable laparoscopic cameras were developed in [4]–[7] with magnetic fixation and positioning.

To improve surgical experiences, researches have focused on developing automatic actuation mechanisms for an insertable laparoscopic camera. One major challenge to design such a camera system is the development of its actuation functions, which are (1) fixation that holds the cameras in stable positions; (2) translation that repositions the cameras; and (3) rotation that manipulates the cameras to desired orientations. The existing laparoscopic camera designs have addressed separate or partial-function-combined actuation mechanisms. A tethered laparoscopic camera, which can be fixed against an abdominal wall by suturing, used two DC motors and peripheral mechanisms for its rotation control [8]. A wireless laparoscopic camera with a needle for fixation was developed to actuate its rotational function (pan and tilt motion) by using two on-board motors [9]. Due to the repositioning difficulty by the fixations of suturing and needle piercing, magnetic anchoring was applied to address this issue. External permanent magnets (EPMs) were utilized to couple with internal permanent magnets (IPMs) inside cameras for fixation, translation and pan motion, while on-board motors were reserved to generate tilt motion [10]–[12].

Researches so far have addressed separate mechanisms with on-board motors for anchoring, translating, and rotating robotic insertable laparoscopic cameras. However, the on-board motors require not only complex peripheral mechanisms that result in bulky articulated designs, but also consume extra on-board power which leads to short battery life for a wireless camera design. There is a need to develop a unified, motor-free, automatic actuation mechanism for a wireless insertable laparoscopic camera.

This paper proposes the final design and a successful prototype of an innovative motor-free actuation mechanism for wireless laparoscopic capsule robots based on our prior work [13], [14]. As illustrated in Fig. 1, the key component and novelty of the capsule robot is the permanent magnetic driving unit, which is referred to as a rotor, driven externally by a specially designed magnetic stator. The rotor, consisting of three IPMs that are distributed at tail-ends and central housing of the capsule robot, can be magnetically coupled to a stator placed externally against or close to the dermal surface. The fixation, translation, and rotation functions of the rotor can be achieved by adjusting the magnetic field from the stator.

Our first design proposed a spherically arranged rotor and stator [13]. Although the design benefited from the small capsule size and simple fabrication, more than 5 A current inputs of the stator coils are required for stable motion control, and resulted in coil overheating. To overcome this issue, a line-arranged rotor and flat arranged stator design was conceptually proposed and validated in simulation [14]. The subsequent experimental validation showed that the robot control with 17 stator coils required a complex algorithm which degraded the control reliability for a practical application.

The contributions of this paper beyond our prior work include: 1) a novel motor-free unified actuation mechanism as the final design that combines EPMs and coils in the stator to provide reliable actuation capabilities for the robot; 2) analytical models and control strategy of the final design for the robot tilt motion control; and 3) a demonstration of the fabricated prototype, with an investigation of the robot actuation capabilities under controlled experimental

[1]Xiaolong Liu and Jindong Tan are with Department of Biomedical Engineering, University of Tennessee, Knoxville, TN 37996, USA xliu57@utk.edu,tan@utk.edu

[2]Gregory J. Mancini is with Graduate School of Medicine, University of Tennessee, TN 37996, USA GMancini@mc.utmck.edu

978-1-4799-9994-1/15/$31.00 ©2015 IEEE

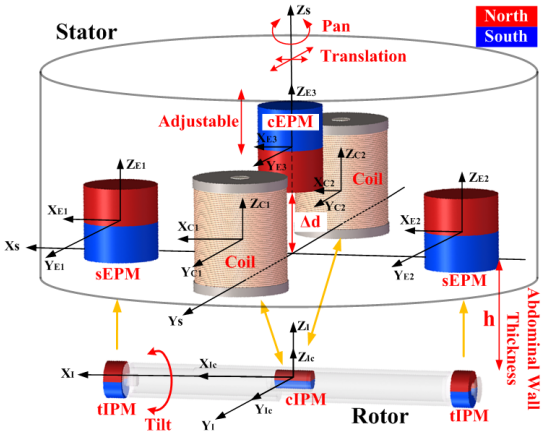

Fig. 1. Conceptual illustration of the locomotion mechanism for the camera robot.

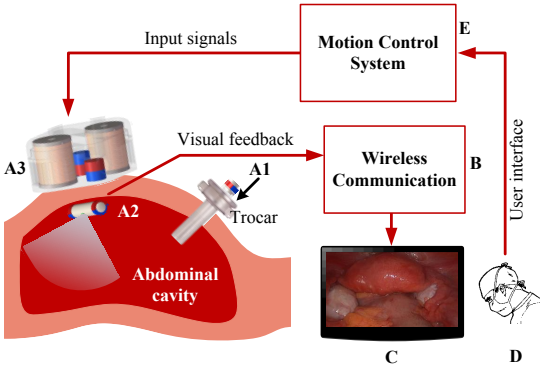

Fig. 2. Application scenario of the laparoscopic capsule camera robot.

environments.

II. Conceptual Design and Application Scenario

A. Conceptual Design

The objective is to design a unified active locomotion mechanism for a fully insertable wireless laparoscopic camera robot with no motor on-board. As conceptually illustrated in Fig.1, the locomotion mechanism consists of (1) a rotor with two tail-end IPMs (tIPMs) and one central IPM (cIPM), and (2) a stator with two coils, two side EPMs (sEPMs), and one central EPM (cEPM). In the stator that placed externally against an abdominal wall, the EPMs and the coils are orthogonally arranged. In the rotor that pushed against an abdominal wall internally, the robot body can rotate freely related to the ring-shaped tIPMs , and the diametrically magnetized cylindrical cIPM is fixed with the robot body.

The stator-rotor mechanism is designed to enable orientation (rotational control), navigation (translational control), in addition to the compensation of the gravity of the camera (fixation control). The robot orientation consists of pan motion and tilt motion. The pan motion requires torque along Z_I axis of the robot, and the tilt motion control requires torque along X_I axis. The robot navigation requires forces along X_I, Y_I, Z_I axes, with the force along Z_I axis providing fixation of the robot against the abdominal wall. The robot navigation control is provided by moving the stator along the dermal surface with the attractive forces between the sEPMs and the tIPMs. A spinning motion of the stator along Z_S can actuate the robot pan motion by coupling the magnetic field of the sEPMs and the tIPMs. Due to the dominated magnetic field from the sEPMs at the location of the cIPM, the cEPM with its north pole pointing downside is used to eliminate the influence from the sEPMs on the cIPM by adjusting the cEPM displacement along Z_S. In this way, the robot tilt motion can be effectively actuated by the magnetic coupling between the coils and the cIPM.

The open-ended research problem of this paper is twofold: (1) the optimal vertical displacements of the cEPM Δd with respect to different abdominal wall thicknesses h; and (2) the control model of the robot tilt motion. The detailed discussion is presented in Section III.

B. Application Scenario

Fig. 2 illustrates an application scenario of the proposed laparoscopic camera robot. To insert the camera robot (A1) into the patient's abdominal cavity, a trocar is firstly applied. The robot is introduced into the abdominal cavity with surgical forceps, and fixed against the abdominal wall at an initial position (A2) by a stator (A3). A surgeon (D) sends signals of desired robot poses to the motion control system (E) by using a user interface. The camera robot at (A2) sends imaging information to the display terminal (C) through the wireless communication module (B).

III. Modeling of Locomotion Mechanism

This section aims at developing an analytical control model to generate appropriate magnetic fields from the stator for the tilt motion of the rotor. The goal can be achieved by solving two problems: first, the EPMs should generate the least magnetic coupling with the cIPM by identifying optimal vertical displacements of the cEPM with respect to different abdominal thicknesses; and second, the robot dynamics for the tilt motion control should be modeled by considering the magnetic force and torque between the stator and the rotor, and the frictional force and torque between the rotor and an abdominal wall.

To clarify the relationship between the stator and the rotor, coordinate systems are defined in Fig. 1, and explained as follows:

- $\Sigma_{Ei}\{X_{Ei}, Y_{Ei}, Z_{Ei}\}$ represent the coordinate systems of the EPMs, $i = 1,2,3$.
- $\Sigma_{Ci}\{X_{Cj}, Y_{Cj}, Z_{Cj}\}$ represent the coordinate systems of the coils, $j = 1,2$.
- $\Sigma_S\{X_S, Y_S, Z_S\}$ and $\Sigma_I\{X_I, Y_I, Z_I\}$ represent the internal coordinates of the stator and the rotor respectively.
- $\Sigma_{Ic}\{X_{Ic}, Y_{Ic}, Z_{Ic}\}$ represents the body attached coordinate systems of the cIPM.

A. Optimal Vertical Displacement of cEPM

The criteria of the optimal vertical displacement Δd of the cEPM is to minimize the magnetic field generated by the

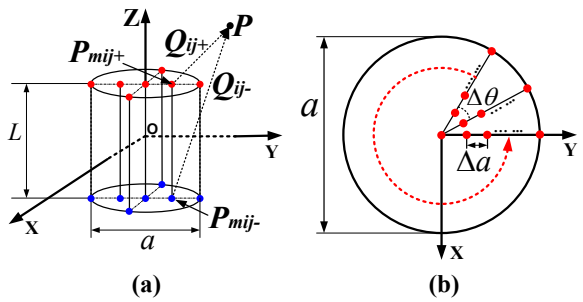

Fig. 3. Unified magnetic field model. (a) The multiple-pair magnetic dipoles. The magnetized direction is along +Z axis. L represents the distance between positive and negative magnetic charges. a represents the diameter of the cylinder space where the magnetic dipoles are distributed. (b) The magnetic charge distribution on the positive charge surface. The magnetic charge sampling line on +Y axis with Δa interval distance rotates around Z axis with an interval angle $\Delta\theta$.

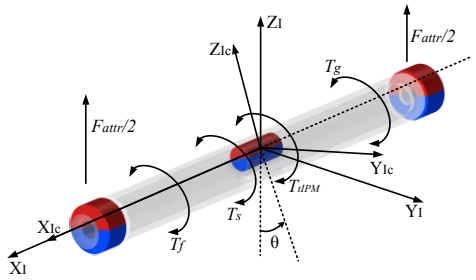

Fig. 4. Dynamic analysis of the robot tilt motion.

three EPMs at the location of the cIPM. Since the location of the cIPM with respect to the stator is determined by an abdominal wall thickness h, the objective is to develop a function for Δd with h as the variable.

1) Magnetic Field Analysis of the Stator: Due to the fixed relative positions of the EPMs and the coils, the stator magnetic field can be calculated by superimposing the magnetic fields from the EPMs and the coils [14]. The whole stator magnetic field $\mathbf{B}_s \in \mathbb{R}^{3\times1}$ in Σ_S is formulated as

$$\mathbf{B}_s(\mathbf{P}_s) = \sum_{i=1}^{3} \mathbf{R}_{Ei}\mathbf{B}_e^i + \sum_{j=1}^{2} \mathbf{R}_{Cj}\mathbf{B}_c^u I_{cj}, \tag{1}$$

where $\mathbf{B}_e^i \in \mathbb{R}^{3\times1}$ denotes the magnetic flux density of the i^{th} EPM in Σ_{Ei}; $\mathbf{B}_c^u \in \mathbb{R}^{3\times1}$ represents the magnetic flux density of an iron-core coil with unit current in Σ_{Cj}; I_{cj} are the coil current inputs; $\mathbf{P}_s$ represents a spacial point in Σ_S; $\mathbf{R}_{Ei} \in \mathbb{R}^{3\times3}$ and $\mathbf{R}_{Cj} \in \mathbb{R}^{3\times3}$ represent the rotational matrices from Σ_S to Σ_{Ei} and from Σ_S to Σ_{Cj} respectively.

Assume that $\mathbf{P}_s = (0,0,-h)^T$ is the location of the cIPM in Σ_S and the coils are deactivated with $I_{cj} = 0$. According to (1), the objective function that characterizes the optimal vertical displacement Δd can be represented as

$$\mathbf{B}_s(0,0,-h) = \sum_{i=1}^{2} \mathbf{R}_{Ei}\mathbf{B}_e^i + \mathbf{R}_{E3}\mathbf{B}_e^3(\mathbf{P}_3) = \mathbf{0}, \tag{2}$$

where $\mathbf{P}_3 = \mathbf{R}_{C3}^T(0,0,-h-\Delta d)^T$ is the point $\mathbf{P}_s = (0,0,-h)^T$ represented in Σ_{E3}; $\mathbf{B}_e^3$ represents the magnetic flux density of the cEPM.

2) Unified Analytical Model of $\mathbf{B}_e^i$ and $\mathbf{B}_c^u$: The representation of the stator magnetic field in (1) and the identification of the relationship between Δd and h in (2) both require analytical models of the EPMs and the coils. Inspired by [15], $\mathbf{B}_e^i$ and $\mathbf{B}_c^u$ can be represented in a unified multi-pair magnetic dipole model due to the cylinder shape of the EPMs and the coils. Compared with a single-pair magnetic dipole model applied in [14], a multi-pair magnetic dipole model has more abilities to achieve an accurate magnetic field estimation.

The unified magnetic field model is illustrated in Fig. 3. The positive and negative magnetic charges are distributed on the top and bottom surfaces of the cylinder in Fig. 3(a). Fig. 3(b) shows the arrangement of magnetic charges on the positive surface. Because the magnetic charges are symmetrically distributed around Z axis, only a quarter values of the magnetic dipoles need to be estimated by using numerical magnetic field data. By summarizing all the magnetic dipoles, the magnetic flux density $\mathbf{B}_0 \in \mathbb{R}^{3\times1}$, which can be used as $\mathbf{B}_e^i$ or $\mathbf{B}_c^u$, is expressed by

$$\mathbf{B}_0 = \frac{\mu_0}{4\pi} m_0 \Gamma_{00} + \frac{\mu_0}{4\pi} \sum_{i=1}^{K_m} \sum_{j=1}^{N_m} m_{ij}\Gamma_{ij}, \tag{3}$$

$$\Gamma_{ij} = \mathbf{Q}_{ij+}/|\mathbf{Q}_{ij+}|^3 - \mathbf{Q}_{ij-}/|\mathbf{Q}_{ij-}|^3, \tag{4}$$

where m_{ij} is the strength of the ij^{th} magnetic dipole, and m_0 is the strength of the magnetic dipole at the center; K_m denotes the number of magnetic dipoles radially, and N_m is the number of magnetic dipoles for a single loop; $\mathbf{Q}_{ij+/-}$ represents a vector from the location of positive/negative magnetic charge $\mathbf{P}_{mij+}/\mathbf{P}_{mij-}$ to a point $\mathbf{P}$ in space.

3) Optimal Displacement $\Delta d = f(h)$: Due to the highly nonlinear property of (2), it is difficult to explicitly represent Δd with h as the variable. An alternative way to develop this function is to build a lookup table by giving a range of abdominal wall thickness values h. After searching for Δd that satisfy (2), the optimized Δd values are stored in the lookup table. To this end, the optimal vertical displacement of cEPM Δd can be identified in real time for different abdominal wall thicknesses h.

B. Control With Electromagnetic Coils

The robot tilt motion is activated by the magnetic coupling between the coils and the cIPM. I_{c1} and I_{c2} are represented as the current inputs of the coils, and θ is represented as the rotational angle of the robot tilt motion. The robot dynamics need to be studied for developing the relationship between the control inputs I_{c1}, I_{c2} and the output θ.

Fig. 4 shows the dynamic analysis of the robot tilt motion. The torques that affect the tilt motion along X_I include (1) T_s which is the magnetic torque on the cIPM from the coils and the EPMs of the stator; (2) T_{tIPM} which is the magnetic torque on the cIPM from the tIPMs along X_I; (3) T_f and T_g which are the frictional torque of the robot-tissue interaction

and the torque due to the robot gravity along X_I. The bold fonts $\mathbf{T}_s, \mathbf{T}_{tIPM}, \mathbf{T}_f$, and $\mathbf{T}_g$ are used to represent the torque vectors with the components along X_I, Y_I, Z_I.

We assume the cIPM is described by a body-attached magnetic moment $\mathbf{M} \in \mathbb{R}^{3\times1}$ with a constant magnitude in ampere square meter. The torque on the cIPM generated from the stator, in newton meters, can be expressed as

$$\mathbf{T}_s = \mathbf{M} \times (\mathbf{R}_S^I \mathbf{B}_s), \tag{5}$$

where $\mathbf{R}_S^I \in \mathbb{R}^{3\times3}$ represents a rotational matrix that transfers $\mathbf{B}_s$ from Σ_S to Σ_I [16]. According to the setting of Σ_S and Σ_I in Fig. 1, $\mathbf{R}_S^I$ is an identity matrix. Combined with (1), (5) can be further represented as

$$\mathbf{T}_s = \underbrace{\mathbf{M} \times (\sum \mathbf{R}_{Ei} \mathbf{B}_e^i)}_{\mathbf{E}} + \underbrace{(\mathbf{M} \times \mathbf{R}_{C1} \mathbf{B}_c^u)}_{\mathbf{C}_1} I_{c1} + \underbrace{(\mathbf{M} \times \mathbf{R}_{C2} \mathbf{B}_c^u)}_{\mathbf{C}_2} I_{c2}, \tag{6}$$

where $\mathbf{E} \in \mathbb{R}^{3\times1}$ denotes the torque from the EPMs, i=1,2,3; $\mathbf{C}_1 \in \mathbb{R}^{3\times1}$ and $\mathbf{C}_2 \in \mathbb{R}^{3\times1}$ denote the unit current torques from the coils. Benefiting from the analytical magnetic field model in (3), $\mathbf{E}$, $\mathbf{C}_1$, and $\mathbf{C}_2$ can be computed in real time.

The non-zero components in $\mathbf{T}_f$ and $\mathbf{T}_{tIPM}$ are the x-components represented by T_f and T_{tIPM}. T_f is determined by F_{attr} as illustrated in Fig. 4, which is the attractive force from the magnetic coupling of the tIPMs and the EPMs. As $F_{attr} = f_1(h)$ and $T_{tIPM} = f_2(\theta)$ are functions of an abdominal wall thickness h and the robot tilt angle θ respectively, f_1 and f_2 can be modeled by polynomial approximation

$$f_1(h) = \sum_{k=1}^{n+1} \eta_k h^{n-k+1}, \quad f_2(\theta) = \sum_{k=1}^{m+1} \xi_k \theta^{m-k+1}, \tag{7}$$

where η_k and ξ_k are the polynomial coefficients to be determined by experimental data; n and m denote the orders of f_1 and f_2.

By representing $\boldsymbol{\omega} = [\dot{\theta}, 0, 0]^T$ as the angular velocity of the robot tilt motion, the dynamic model can be formulated in Σ_I as

$$\mathbf{T}_s + \mathbf{T}_{tIPM} + \mathbf{T}_f + \mathbf{T}_g = \mathbf{I}'\dot{\boldsymbol{\omega}} + \boldsymbol{\omega} \times \mathbf{I}'\boldsymbol{\omega}, \tag{8}$$

where $\mathbf{I} \in \mathbb{R}^{3\times3}$ is the moment of inertia in the body attached frame Σ_{I_c}; $\mathbf{R}_I^{I_c} \in \mathbb{R}^{3\times3}$ is the rotational matrix from Σ_I to Σ_{I_c}; $\mathbf{I}' = \mathbf{R}_I^{I_c} \cdot \mathbf{I} \cdot (\mathbf{R}_I^{I_c})^T$ is the moment of inertia of the rigid body in Σ_I.

Since the tilt motion is actuated along the X_I axis, only the x components need to be considered in (8). By substituting (6) and (7) in (8), the dynamic equation is reformulated as

$$E_x + C_{1x} I_{c1} + C_{2x} I_{c2} + T_{tIPM} + \mu(F_{attr} - mg) r_f + mg r_g \sin\theta = a_{11}\ddot{\theta}, \tag{9}$$

where E_x, C_{1x}, C_{2x} are the x components in $\mathbf{E}, \mathbf{C}_1$, and $\mathbf{C}_2$ respectively; μ is the frictional coefficient between the robot and an abdominal wall; mg represents the gravity of the robot; r_f and r_g denote the lever arms of the friction force and the gravity force to generate T_f and T_g; a_{11} denotes the element of 1^{th} row, 1^{th} column in $\mathbf{I}$;

To generate a desired tilt angle for the robot, the coil current inputs I_{c1} and I_{c2} can be found by applying pseudoinverse to

$$\mathbf{C}_x \mathbf{I}_c = G, \tag{10}$$

where $\mathbf{C}_x = [C_{1x}, C_{2x}] \in \mathbb{R}^{1\times2}$; $\mathbf{I}_c = [I_{c1}, I_{c2}]^T \in \mathbb{R}^{2\times1}$; G represents the summation of the remaining terms in (9). Because $\mathbf{C}_x$ has a full row rank, the solution of the current input vector $\mathbf{I}_c$ can be calculated by using

$$\mathbf{I}_c = \mathbf{C}_x^T (\mathbf{C}_x \mathbf{C}_x^T)^{-1} G. \tag{11}$$

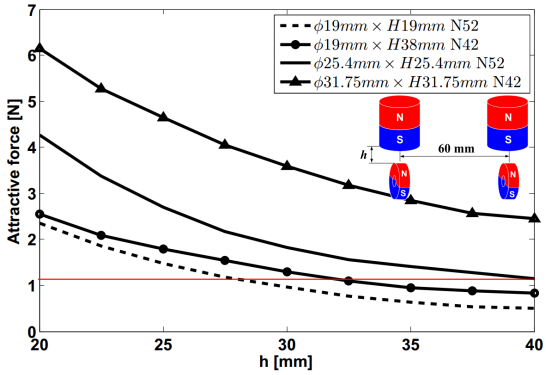

Fig. 5. Attractive force between sEPM candidates and the tIPMs.

IV. Prototype Development and Experimental Validation

In this section, COMSOL Multiphysics 5.0 (COMSOL Inc., Sweden) was used as the measurement tool of magnetic forces and torques for the stator and rotor design, and the benchmark for evaluating the analytical models in Section III.

A. Robot Fabrication and Experimental Environment Setup

1) Rotor design: To compromise between reserving sufficient space for on-board electronics and a compact robot design, the robot was fabricated with the dimensions of 68 mm in length and 12.7 mm in diameter. The IPMs applied in the robot design were diametrically magnetized with the material of NdFeB Grade N42 (K&J Magnetics Inc.). The tIPMs were ring-shaped magnets with dimensions of 12.7 mm outer diameter (OD), 4.76 mm inner diameter (ID), and 6.35 mm thickness. The cIPM is a cylindrical magnet with dimensions of 6.35 mm diameter and 12.7 mm thickness. The total weight of the robot was estimated as less than 30 g by considering the candidate on-board electronics.

2) Stator design: The stator design follows three steps to enable sufficient actuation capabilities: (1) sEPMs selection; (2) cEPM selection; and (3) coils design. Fig. 5 shows the attractive force between the tIPMs and the candidate sEPMs which are off-the-shelf permanent magnets (K&J Magnetics Inc.). Under various abdominal wall thicknesses h, the magnet with the dimension $\phi25.4$ mm $\times$ $H25.4$ mm,

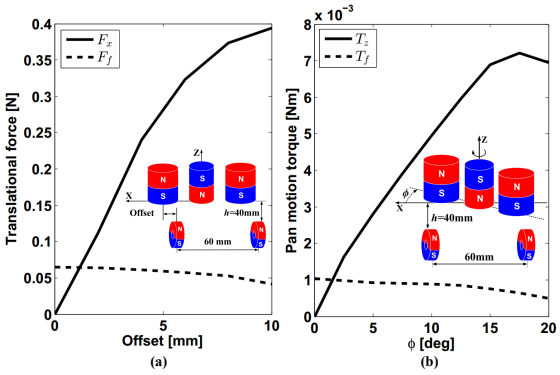

Fig. 6. Translational force and pan motion torque investigation. (a) The comparison result of translational force F_x in X direction, and frictional force F_f in -X direction with the stator offset distance 0 ~ 10 mm. (b) The comparison result of pan motion torque T_z and frictional torque T_f.

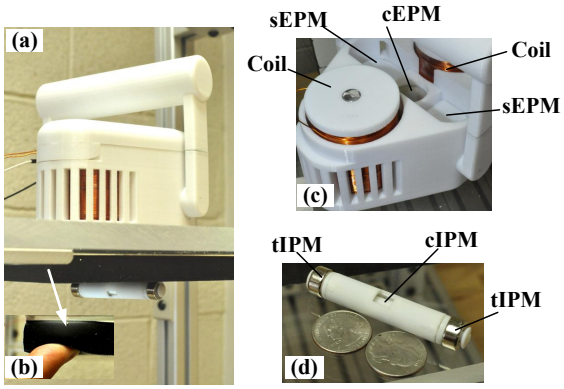

Fig. 7. Experimental environment and the fabricated capsule robot system: (a) experiment setups for evaluating the robot locomotion capabilities; (b) the simulated abdominal wall tissue made by a viscoelastic material; (c) the stator design; (d) the rotor design.

which generated more than 4 N force at $h = 20$ mm and 1 N at 40 mm, provided reliable fixation force without causing undesired histological damages [18].

The cEPM was selected as an axially magnetized cylindrical magnet with 22.22 mm diameter, 28.57 mm height to reduce the magnetic field on the cIPM from the sEPMs. Fig. 6(a) shows that the translational force F_x in X direction can overcome the frictional force F_f in -X direction under 40 mm abdominal wall thickness. Fig. 6(b) shows the pan motion torque T_z from the EPMs can overcome frictional torque T_f after a relative rotational angle $\phi = 2°$ was reached.

The dimensions of the coils were determined as 50 mm height, 50 mm OD, 10 mm ID, and iron cores with 60 mm length based on trial-and-error experiments, which indicated the dimensions compromised compact coil size with sufficient strength of magnetic field. The winding wire in the coils were AWG23 copper wire with 2,000 turns (TEMCo Inc.). The iron cores are made by EFI Alloy 50 from Ed Fagan with maximum permeability 10,000. For the safety consideration, the coil input current is limited to 1.5 A for preventing coil overheating.

3) Current control system: A tethered current control system was developed by the PWM technique. The system consists of a micro-controller (STM32F4Discovery, STMicroelectronics Inc.) to generate PWM signals, two PWM amplifiers (L6205 DMOS Full Bridge Driver, STMicroelectronics Inc.) to amplify the signals, a power supply for powering up the amplifiers, and a PC computer to send control command to the micro-controller via a serial communication.

4) Experiment platform setup: Fig. 7(a) shows the overview of the experimental environment. The robot system was fabricated by a 3D prototyping machine (Fortus 400mc, Stratasys Inc.). To simulate the viscoelastic properties of a real insufflated abdominal wall (average Young's modulus 32.5 kPa) [17], a viscoelastic material Durometer 40 with (Young's modulus 27.57 kPa at 15% deflection, Sorbothane, Inc.) was applied as illustrated in Fig. 7(b). The initial abdominal wall thickness was 26 mm (tissue layer 15 mm, support layer 11 mm), which can be adjusted by increasing

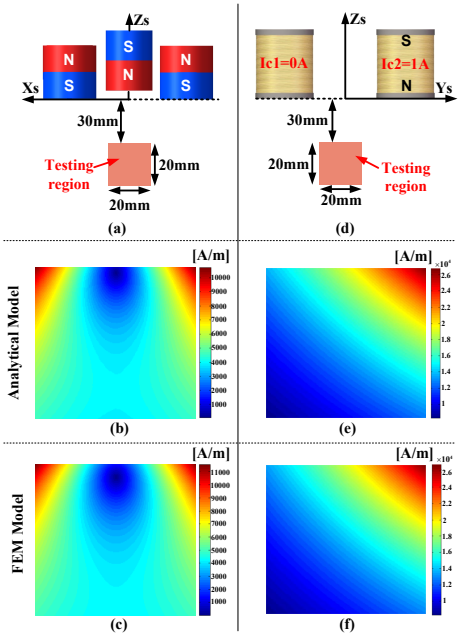

Fig. 8. Stator magnetic field model evaluation. (a) The testing region of the EPMs. (b)-(c) The EPMs magnetic fields generated by the analytical model and a FEM model separately. (d) The testing region of the coils. (e)-(f) The magnetic fields of the coil in the testing region. (e) and (f) were generated by the analytical model a FEM model respectively.

the distance between the stator and the support layer. The vertical displacement Δd of the cEPM can be manually adjusted at this stage. A lubricated rotor-tissue contact layer was added to the bottom of the viscoelastic material for mimicking an internal abdominal wall surface.

B. Analytical Model Evaluation

1) Stator magnetic field: Fig. 8 shows the experimental validation for the stator magnetic field model developed in (1) and (3). Considering the working space of the cIPM, 20 mm × 20 mm magnetic field testing regions were designed on both the $X_S Z_S$ plane and the $Z_S Y_S$ plane for validating the EPM field and the coil field respectively as illustrated in

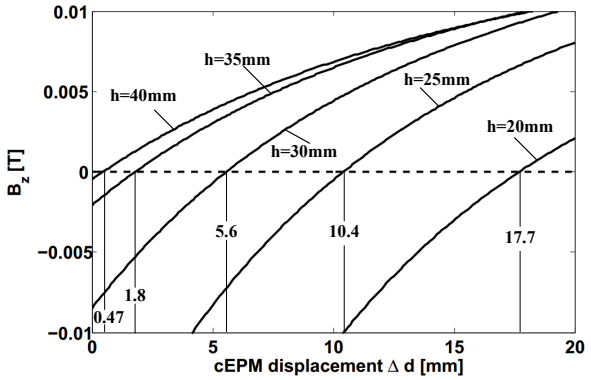

Fig. 9. Optimal vertical displacements of the cEPM for different abdominal wall thicknesses.

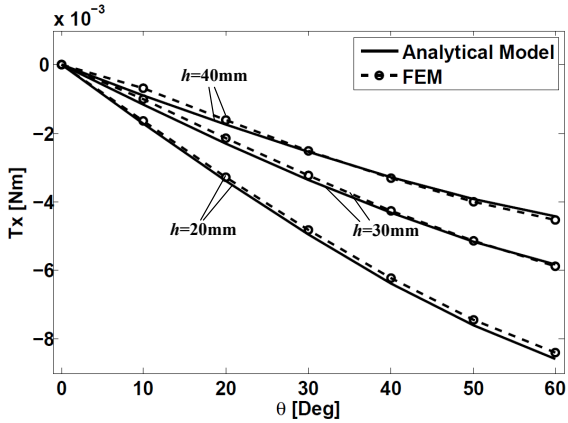

Fig. 10. Evaluation of the analytical torque model on the cIPM. The torques calculated by FEM models serve as benchmarks to compare with the torques generated by the analytical model in (6) under different abdominal wall thicknesses.

Fig. 8(a) and (d). The vertical displacement of the cEPM was set as $\Delta d = 5$ mm for Fig. 8(a) and the coil current inputs were set as $I_{c1} = 0, I_{c2} = 1$ A for Fig. 8(d). The comparison results of the magnetic field maps generated by the analytical model and a finite element model (FEM) indicated that the developed analytical models can achieve accurate magnetic field maps.

2) Optimal displacement function of Δd: The optimal vertical displacements of the cEPM Δd, which are the solutions to (2), are illustrated in Fig. 9 by giving several abdominal wall thicknesses h. Since the only non-zero component of the stator magnetic field along Z_S axis is B_z when the coils are deactivated, the optimal Δd can be found by searching for the one that makes $B_z = 0$. Fig. 9 shows the optimal $\Delta d = 17.7$ mm when $h = 20$ mm and $\Delta d = 0.47$ mm when $h = 40$ mm.

3) Magnetic torque on the cIPM: Fig. 10 shows the evaluations of the analytical model developed in (6) by setting abdominal thicknesses as $h = 20$ mm, 30 mm, and 40 mm. The magnetic torque on the cIPM was generated by fixing the coil current inputs as $I_{c1} = 1$ A and $I_{c2} = 1$ A, while changing the cIPM tilt angle θ from 0° to 60°. The average error between the analytical model and the FEM

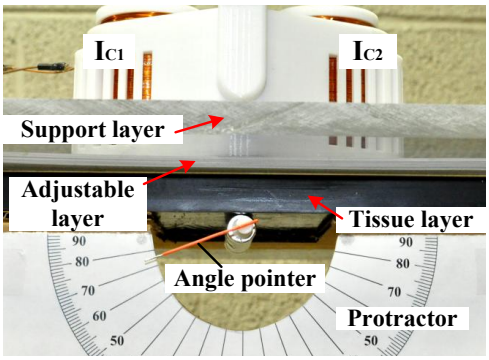

Fig. 11. Tilt angle measurement. I_{c1} and I_{c2} are the coil current inputs.

model is 4.58%. The results also validate the assumption we made for developing (5).

4) Polynomial coefficients: The experiment data for estimating the polynomial coefficients in (7) were acquired from FEM models developed in COMSOL. The orders of f_1 and f_2 were determined as $n = 3$ and $m = 5$ with average errors 0.16% and 0.48% respectively. The coefficients were estimated as $\eta_1 = -0.0925$, $\eta_2 = 0.252$, $\eta_3 = -0.603$, $\eta_4 = 1.196$ for f_1, and $\xi_1 = -2.66\times10^{-5}$, $\xi_2 = -2.55\times10^{-5}$, $\xi_3 = 4.45 \times 10^{-4}$, $\xi_4 = 1.13 \times 10^{-4}$, $\xi_5 = -2.42 \times 10^{-3}$, $\xi_6 = -4.91 \times 10^{-5}$ for f_2.

C. Experimental Validation

1) Range of Tilt Motion: To measure the range of the robot tilt motion, I_{c1} and I_{c2} were initially set at their maximum 1.5 A. Then I_{c1} was linearly changed from 1.5 A to −1.5 A in 5 s. To indicate the tilt angles, a protractor and an angle pointer were applied as shown in Fig. 11. The maximum achievable tilt angles with abdominal wall thickness 26 mm and 40 mm were measured as 72° and 78° by setting Δd at 9 mm and 0 mm respectively.

2) Open-loop Control of Tilt Motion: Due to the lack of on-board inertial sensing at this stage, an open-loop control of the robot tilt motion was implemented by (9) and (11). The total thickness of the simulated abdominal wall was configured as $h = 30$ mm. Considering the candidate on-board electronics that will be integrated in the robot, the moment of inertia matrix $\mathbf{I}$ of the robot was estimated by modeling it in SolidWorks2013 (Dassault Systémes SolidWorks Corp.) as

$$\mathbf{I} = \begin{pmatrix} 0.174 & 0 & -0.003 \\ 0 & 3.473 & 0 \\ 0 & 0 & 3.469 \end{pmatrix}, \quad (12)$$

where the unit of each element in $\mathbf{I}$ is kg mm^2. The other parameters used in (9) were estimated or measured as $\mu = 0.1$, $r_f = 4$ mm, $r_g = 1.5$ mm, and $mg = 0.26$ N.

Fig. 12 shows the experimental results of the current inputs I_{c1} and I_{c2} (Fig. 12(a)-(c)), target angle θ_d (red lines in Fig. 12(d)-(f)), and output tilt angle θ (blue lines in Fig. 12(d)-(f)). Three 5th-order desired trajectories, which are smooth at the angular acceleration level, were generated by initializing the robot tilt angles as 0° and setting the

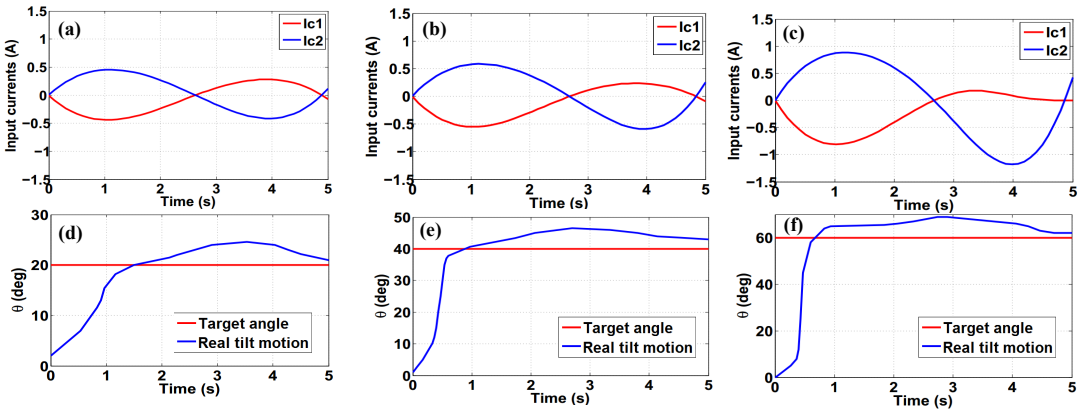

Fig. 12. Open-loop control of tilt motion. (a-c) Current inputs of I_{c1} and I_{c2}. (d-f) Target tilt angles and real tilt motion trajectories.

target angles as 20°, 40° and 60°. The generated tilt motion trajectories were recorded by a video recorder (D90 SLR Camera, Nikon Corp.) with a capture speed of 24 frames-per-second. The results validate the tilt motion control model proposed in Section III-B.

V. Conclusion and Future Work

In this paper, a novel locomotion mechanism for an insertable laparoscopic camea is presented, which features a unified control for fixation, translation and rotation. The experiments showed that the system provides reliable anchoring, translation, 360° continuous pan motion control, and fine tilt motion control with at least a 72° maximum tilt angle under the conditions of 26 mm ~ 40 mm simulated abdominal wall thicknesses. Pan and tilt motion can be simultaneously controlled in a decoupled way, which enables a flexible motion control of the capsule robot to illuminate and visualize a target surgical area.

In our future work, an abdominal wall thickness sensing system will be developed and integrated in the stator. The vertical displacement Δd will be automatically adjusted in accordance with the sensed h. The camera on-board electronics will also be integrated. Instead of manually generating the robot pan motion, an automatic mechanism will be designed, which actuates the camera pan motion by control signals from surgeons.

References

[1] M. Desai, A. Berger, R. Brandina, M. Aron, B. Irwin, D. Canes, M. Desai, P. Rao, R. Sotelo, R. Stein, and I. Gill, "Laparoendoscopic single-site surgery: Initial hundred patients," *Urology*, vol. 74, no. 4, pp. 805 – 812, 2009.

[2] M. Saidy, M. Tessier, and D. Tessier, "Single-incision laparoscopic surger–hype or reality: A historical control study," *Perm J.*, vol. 16, no. 1, pp. 47–50, 2012.

[3] C. Tracy, J. Raman, J. A. Cadeddu, and A. Rane, "Laparoendoscopic single-site surgery in urology: where have we been and where are we heading?," *Nat Clin Pract Urol.*, vol. 5, no. 10, pp. 561–568, 2008.

[4] M. Fakhry, B. Gallagher, F. Bello, and G. Hanna, "Visual exposure using single-handed magnet-driven intra-abdominal wireless camera in minimal access surgery: is better than 30 degrees endoscope.," *Surg Endosc.*, vol. 23, no. 3, pp. 539–543, 2009.

[5] P. Swain, R. Austin, K. Bally, and R. Trusty, "Development and testing of a tethered, independent camera for notes and single-site laparoscopic procedures.," *Surg Endosc.*, vol. 24, no. 8, pp. 2013–21, 2010.

[6] J. Cadeddu, R. Fernandez, M. Desai, R. Bergs, C. Tracy, S. Tang, P. Rao, M. Desai, and D. Scott, "Novel magnetically guided intra-abdominal camera to facilitate laparoendoscopic single-site surgery: initial human experience.," *Surg Endosc.*, vol. 23, no. 8, pp. 1894–9, 2009.

[7] M. Silvestri, T. Ranzani, A. Argiolas, M. Vatteroni, and A. Menciassi, "A multi-point of view 3d camera system for minimally invasive surgery," *Sensors and Actuators A: Physical*, vol. 202, pp. 204 – 210, 2013.

[8] T. Hu, K. Allen, J. Hogle, and L. Fowler, "Insertable surgical imaging device with pan, tilt, zoom, and lighting," *The International Journal of Robotics Research*, vol. 28, no. 10, pp. 1373–1386, 2009.

[9] C. Castro, S. Smith, A. Alqassis, T. ketterl, S. Yu, S. Ross, A. Rosemurgy, P. Savage, and R. Gitlin, "A wireless robot for networked laparoscopy," *Biomedical Engineering, IEEE Transactions on*, vol. 60, no. 4, pp. 930–936, 2013.

[10] S. Platt, J. Hawks, and M. Rentschler, "Vision and task assistance using modular wireless in vivo surgical robots," *Biomedical Engineering, IEEE Transactions on*, vol. 56, no. 6, pp. 1700 –1710, 2009.

[11] M. Simi, M. Silvestri, C. Cavallotti, M. Vatteroni, P. Valdastri, A. Menciassi, and P. Dario, "Magnetically activated stereoscopic vision system for laparoendoscopic single-site surgery," *Mechatronics, IEEE/ASME Transactions on*, vol. 18, no. 3, pp. 1140–1151, 2013.

[12] M. Simi, G. Sardi, P. Valdastri, A. Menciassi, and P. Dario, "Magnetic levitation camera robot for endoscopic surgery," in *Robotics and Automation (ICRA), 2011 IEEE International Conference on*, pp. 5279–5284, 2011.

[13] X. Liu, G. Mancini, and J. Tan, "Design of a unified active locomotion mechanism for a capsule-shaped laparoscopic camera system," in *Robotics and Automation (ICRA), 2014 IEEE International Conference on*, pp. 2449–2456, 2014.

[14] X. Liu, G. J. Mancini, and J. Tan, "Design of a unified active locomotion mechanism for a wireless laparoscopic camera system," in *Intelligent Robots and Systems (IROS), 2014 IEEE/RSJ International Conference on*, pp. 1294–1301, 2014.

[15] L. Kok-Meng and S. Hungsun, "Distributed multipole model for design of permanent-magnet-based actuators," *Magnetics, IEEE Transactions on*, vol. 43, no. 10, pp. 3904–3913, 2007.

[16] J. D. Jackson, *Classical electrodynamics*. New York, NY: Wiley, 1999.

[17] C. Song, A. Alijani, T. Frank, G. Hanna, and A. Cuschieri, "Mechanical properties of the human abdominal wall measured in vivo during insufflation for laparoscopic surgery," *Surgical Endoscopy And Other Interventional Techniques*, vol. 20, no. 6, pp. 987–990, 2006.

[18] S. Best, W. Kabbani, D. Scott, R. Bergs, H. Beardsley, R. Fernandez, L. Mashaud, and J. Cadeddu, "Magnetic anchoring and guidance system instrumentation for laparo-endoscopic single-site surgery/natural orifice transluminal endoscopic surgery: lack of histologic damage after prolonged magnetic coupling across the abdominal wall.," *Urology*, vol. 77, no. 1, pp. 243–7, 2011.